

Supporting Information for: Large angle, multi-functional metagratings based on freeform multi-mode geometries

David Sell¹, Jianji Yang², Sage Doshay¹, Rui Yang², and Jonathan A. Fan^{2*}

1. Department of Applied Physics, Stanford University, Stanford, CA 94305
2. Department of Electrical Engineering, Stanford University, Stanford, CA 94305

*Address correspondence to: jonfan@stanford.edu

Contents

1. Fabrication and Experimental Setup
2. Grating design parameters for devices featured in Figure 1a of main text
3. Theory of adjoint-based optimization for metagratings
4. Summary of iterative topology optimization procedure with built-in robustness
5. Coupled Bloch mode theory for grating analysis
6. Mode analysis: Topology-optimized 75 degree deflector
7. Mode analysis: Metagrating deflector based on effective refractive index design concept
8. Incident angle sensitivity of the topology-optimized 75 degree deflector
9. Additional images and experimental spectra of the topology-optimized 75 degree deflector
10. Analysis of the accuracy of rigorous coupled-wave analysis simulations
11. Analysis of the topology-optimized 75 degree deflector using finite-element-method (COMSOL) calculations
12. Geometrical parameters of the metagrating deflectors in Figure 1a
13. Description of Movie S1
14. References

1. Fabrication and Experimental Setup

To fabricate the silicon metagratings, polycrystalline silicon (p-Si) is deposited onto multiple wafers, including fused silica substrates and crystalline silicon structures with a thermal oxide, using silane in a low-pressure chemical vapor deposition furnace at 620°C. The samples consisting of p-Si on thermal oxide on crystalline silicon are optically characterized using ellipsometry to determine the final thickness and the refractive index of the p-Si. A 30nm-thick silicon dioxide hard mask is then deposited by plasma-enhanced chemical vapor deposition. The patterns are defined via electron beam lithography using ZEP 520A resist. The nanostructures are dry-etched using a breakthrough C_2F_6 etch, followed by a Cl_2 , HBr, and O_2 main etch, and finally an HBr and O_2 overetch. Finally, the samples are cleaned in piranha solution.

To characterize the devices, light from an NKT SuperK white light laser is wavelength-filtered using an LLTF module, collimated, and polarized. It is then lightly focused onto the devices using a 0.055 NA objective. The transmitted beam is characterized with a germanium power meter mounted on a motorized rotation stage. A schematic of this setup is shown in Figure S1a. A section of the substrate with the silicon fully etched away is used as a calibration window and serves as a reference region for the total transmitted power from the source.

The angular distribution of the focusing beam is experimentally characterized at wavelengths of 1000nm, 1050nm, and 1300nm, and in all three cases, the angular spread is within ± 1 degree from normal (Figure S1b). The transmitted beam is characterized with a germanium power meter mounted on a motorized rotation stage. A section of the substrate with the silicon fully etched away is used as a calibration window and serves as a reference region for the total transmitted power from the source.

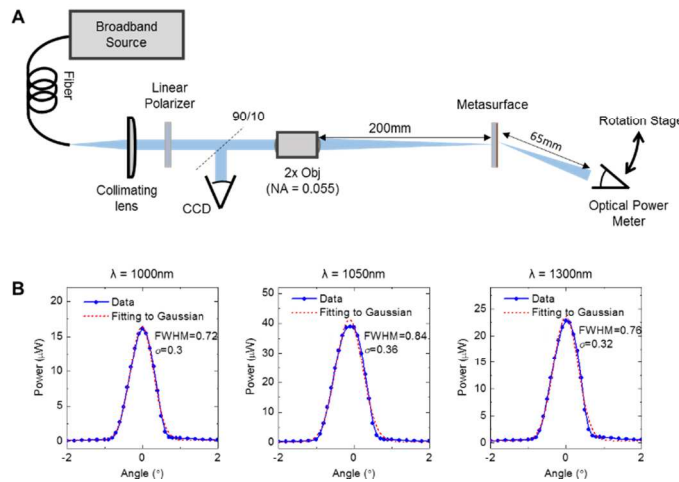


Figure S1. (a) Schematic of the experimental setup. (b) Experimentally measured angular profiles of the incident beam at three different wavelengths.

2. Grating design parameters for devices featured in Figure 1a of main text

The grating designs simulated in Figure 1a of the main text are based on metagrating designs in previously published papers. The material systems, operating wavelengths, and bibliographic sources for these designs are listed in Table S1.

Table S1. Summary of parameters used for simulations in Figure 1a of main text

Grating design approach	Material	Wavelength (nm)	References
Effective medium	TiO ₂	860	P. Lalanne <i>et. al.</i> , <i>J. Opt. Soc. Am. A</i> 16 , 1143-1156, (1999).
Transmit array	poly-Silicon	1550	A. Arbabi <i>et. al.</i> <i>Nat. Comm.</i> 6 , 7069 (2015).
Geometric phase	TiO ₂	405	M. Khorasaninejad <i>et. al.</i> , <i>Science</i> 352 , 1190-1194, (2016).
Echelle (sawtooth profile)	SiO ₂ ($n = 1.45$)	1050	P. Lalanne <i>et. al.</i> , <i>J. Opt. Soc. Am. A</i> 16 , 1143-1156, (1999).

3. Theory of adjoint-based optimization for metagratings

We present in this section the mathematical framework of adjoint optimization that we use in our metagrating inverse design simulations. A general mathematical derivation and description of the adjoint method can be found in optimization textbooks such as Ref. [11]. The adjoint-based optimization method uses only two electromagnetic simulations per iteration to solve for gradients in dielectric constant at all spatial locations in a device. The primary goal of our optimization problem, which includes large angle and multi-functional deflection, is to maximize the transmission efficiency of incident plane waves into targeted diffraction order channels. For a metagrating designed for an incident plane wave with a specific polarization and wavelength, our Figure of Merit (FoM) is defined as the transmission intensity T_m to the desired (m^{th}) diffracted order:

$$\text{FoM} = T_m \quad (\text{S3-1})$$

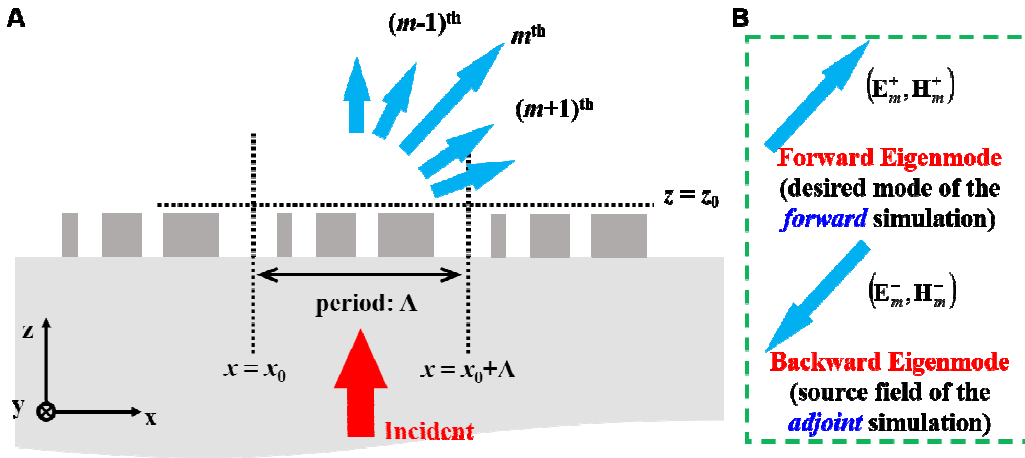


Figure S2. 1D lamellar grating. (a) Configuration of the simulated system. The grating is composed of several dielectric nanobeams. Light is incident on the grating from the substrate and couples into several diffraction orders. (b) Forward and backward eigenmodes. The forward eigenmode represents the desired transmitted diffraction order in the forward simulations, while the backward mode is used for the adjoint simulations. Note that the forward and backward eigenmodes are the same mode, but they propagate in opposite directions.

T_m can be obtained by projecting the total transmitted field to the m^{th} diffraction order. For the sake of illustration, we consider here a plane wave that is normally incident on a 1D lamellar grating through a substrate (Figure S2). The incident power P_{inc} in a single period of the grating is assumed to be 1. The transmission efficiency T_m , normalized relative to the intensity of the incident beam, can be found by performing an overlap integral between two fields: the total field $(\mathbf{E}(x, z_0), \mathbf{H}(x, z_0))$ that is excited by

the incident field, and the desired (m^{th}) diffracted order field $(\mathbf{E}_m^-(x, z_0), \mathbf{H}_m^-(x, z_0))$. In this expression for the diffracted fields, the subscript ‘ m ’ denotes the order of the diffraction channel and the superscript ‘ $-$ ’ indicates that the field is propagating downward in the $-z$ direction (see Figure S2b). Both fields are evaluated at the $z = z_0$ plane above the grating, and the overlap integral is performed for a single grating period Λ :

$$T = |t|^2 = \frac{\left| \int_{x=x_0}^{x=x_0+\Lambda} [\mathbf{E}(x, z_0) \times \mathbf{H}_m^-(x, z_0) - \mathbf{E}_m^-(x, z_0) \times \mathbf{H}(x, z_0)] \cdot \mathbf{n}_z dx \right|^2}{|\mathbf{N}_m|^2}, \quad (\text{S3-2})$$

where $\mathbf{N}_m = \int_{x=x_0}^{x=x_0+\Lambda} [\mathbf{E}_m^+(x, z_0) \times \mathbf{H}_m^-(x, z_0) - \mathbf{E}_m^-(x, z_0) \times \mathbf{H}_m^+(x, z_0)] \cdot \mathbf{n}_z dx$ defines the normalization of the m^{th} diffraction order, and $(\mathbf{E}_m^+(x, z_0), \mathbf{H}_m^+(x, z_0))$ and $(\mathbf{E}_m^-(x, z_0), \mathbf{H}_m^-(x, z_0))$ denotes the fields propagating in the forward ($+z$) and backward ($-z$) directions. This normalization procedure is consistent with the Lorentz reciprocity relation,^{33,34} and it is valid for both lossy (e.g., plasmonic)³⁵ and lossless (e.g., fiber modes or planewaves) eigenmodes. Assuming $|\mathbf{N}_m| = 1$, the FoM can be written as:

$$\text{FoM} = \left| \int_{x=x_0}^{x=x_0+\Lambda} [\mathbf{E}(x, z_0) \times \mathbf{H}_m^-(x, z_0) - \mathbf{E}_m^-(x, z_0) \times \mathbf{H}(x, z_0)] \cdot \mathbf{n}_z dx \right|^2 \quad (\text{S3-3})$$

If we introduce a small perturbation in permittivity $\Delta\epsilon$ within a small volume ΔV at a location $\mathbf{r}_1 = (x_1, z_1)$ in the grating layer, the total field at the $z = z_0$ plane can be described as $[\mathbf{E}(x, z_0) + \Delta\mathbf{E}(x, z_0), \mathbf{H}(x, z_0) + \Delta\mathbf{H}(x, z_0)]$. The new FoM can be written as:

$$\text{FoM}' = \left| \int_{x=x_0}^{x=x_0+\Lambda} \left[(\mathbf{E}(x, z_0) + \Delta\mathbf{E}(x, z_0)) \times \mathbf{H}_m^-(x, z_0) - \mathbf{E}_m^-(x, z_0) \times (\mathbf{H}(x, z_0) + \Delta\mathbf{H}(x, z_0)) \right] \cdot \mathbf{n}_z dx \right|^2 \quad (\text{S3-4})$$

We can simplify this expression by omitting the $O(\Delta^2)$ terms, which is a valid approximation if the change in the field from the dielectric perturbation $\Delta\epsilon$ is sufficiently small. The *change* of the figure of merit resulting from the inclusion of $\Delta\epsilon$ can be found by combining Equations S3-3 and S3-4:

$$\Delta\text{FoM} = \text{FoM}' - \text{FoM} = 2 \text{Re} \left(\text{conj}(t) \int_{x=x_0}^{x=x_0+\Lambda} [\mathbf{E}(x, z_0) \times \mathbf{H}_m^-(x, z_0) - \mathbf{E}_m^-(x, z_0) \times \mathbf{H}(x, z_0)] \cdot \mathbf{n}_z dx \right) \quad (\text{S3-5})$$

The addition of the tiny perturbation $\Delta\epsilon$ at location \mathbf{r}_1 can be treated as the insertion of an electric dipole with dipole moment $\mathbf{p} = \epsilon_0 \Delta\epsilon \Delta v \mathbf{E}_{app}$, where \mathbf{E}_{app} denotes the approximated value of the electric field

inside the perturbation. A rough estimation of \mathbf{E}_{app} is $\mathbf{E}_{app} \approx \mathbf{E}(\mathbf{r}_1)$. This electric dipole produces scattered fields described by:

$$\begin{cases} \Delta \mathbf{E}(x, z_0) = \omega^2 \mathbf{G}_{ep}(\mathbf{r}, \mathbf{r}_1) \mathbf{p} \\ \Delta \mathbf{H}(x, z_0) = \omega^2 \mathbf{G}_{hp}(\mathbf{r}, \mathbf{r}_1) \mathbf{p} \end{cases} \quad (\text{S3-6})$$

where \mathbf{G}_{ep} and \mathbf{G}_{hp} are the Green's tensors. Equation S3-5 can now be written as:

$$\Delta \text{FoM} = 2\omega^2 \varepsilon_0 \Delta \varepsilon(\mathbf{r}_1) \Delta V \text{Re} \left(\text{conj}(t) \cdot \int_{x=x_0}^{x=x_0+\Lambda} \left[\begin{pmatrix} \mathbf{G}_{ep}(\mathbf{r}, \mathbf{r}_1) \mathbf{E}(\mathbf{r}_1) \\ \mathbf{E}_m^-(x, z_0) \end{pmatrix} \times \begin{pmatrix} \mathbf{H}_m^-(x, z_0) \\ \mathbf{G}_{hp}(\mathbf{r}, \mathbf{r}_1) \mathbf{E}(\mathbf{r}_1) \end{pmatrix} \right] \bullet \mathbf{n}_z dx \right) \quad (\text{S3-7})$$

Applying vector identities into Eq. (S3-7), we obtain the gradient of FoM to the local permittivity at $\mathbf{r}_1 = (x_1, z_1)$ as:

$$\left. \frac{\partial \text{FoM}}{\partial \varepsilon} \right|_{r=r_1} = 2\varepsilon_0 \omega^2 \Delta V \text{Re} \left(\text{conj}(t) \mathbf{E}(\mathbf{r}_1) \bullet \int_{x=x_0}^{x=x_0+\Lambda} \left[\begin{pmatrix} \mathbf{G}_{ep}(\mathbf{r}_1, \mathbf{r}) (-\mathbf{n}_z \times \mathbf{H}_m^-(x, z_0)) \\ -\mathbf{G}_{hp}^T(\mathbf{r}_1, \mathbf{r}) (\mathbf{n}_z \times \mathbf{E}_m^-(x, z_0)) \end{pmatrix} \right] dx \right) \quad (\text{S3-8})$$

Note that the term $\left[\mathbf{G}_{ep}(\mathbf{r}_1, \mathbf{r}) (-\mathbf{n}_z \times \mathbf{H}_m^-(x, z_0)) + (-1) \mathbf{G}_{hp}^T(\mathbf{r}_1, \mathbf{r}) (\mathbf{n}_z \times \mathbf{E}_m^-(x, z_0)) \right]$ represents the field induced by an incident field $(\mathbf{E}_m^-, \mathbf{H}_m^-)$ at the location \mathbf{r}_1 . Therefore, Equation S3-8 can be rewritten as:

$$\left. \frac{\partial \text{FoM}}{\partial \varepsilon} \right|_{r=r_1} = 2\varepsilon_0 \omega^2 \Delta V \text{Re}(\text{conj}(t) \mathbf{E}(\mathbf{r}_1) \bullet \mathbf{E}_{\text{adjoint}}(\mathbf{r}_1)) \quad (\text{S3-9})$$

where $\mathbf{E}_{\text{adjoint}}(\mathbf{r}_1) = \left[\mathbf{G}_{ep}(\mathbf{r}_1, \mathbf{r}) (-\mathbf{n}_z \times \mathbf{H}_m^-(x, z_0)) + (-1) \mathbf{G}_{hp}^T(\mathbf{r}_1, \mathbf{r}) (\mathbf{n}_z \times \mathbf{E}_m^-(x, z_0)) \right]$ is defined as the adjoint field and can be obtained by an auxiliary simulation in which the backward-propagating eigenmode $(\mathbf{E}_m^-, \mathbf{H}_m^-)$ serves as the incident field (See Figure S2 and 1c of the main text).

Equation S3-9 indicates that with only two simulations, one forward simulation and one adjoint simulation, $\frac{\partial \text{FoM}}{\partial \varepsilon}$ can be evaluated at all the locations of the device.

4. Summary of iterative topology optimization procedure with built-in robustness

The optimization is performed in an iterative manner and typically takes 200-300 iterations to achieve convergence. It is summarized in the flow chart shown in Figure S3. The starting point is a random dielectric continuum, and over the course of the iterative process, this continuum converges to discrete values of silicon and air. In this section, we discuss our strategy for driving the dielectric continuum to discrete values of silicon and air, and our method for incorporating geometric robustness in our designs.

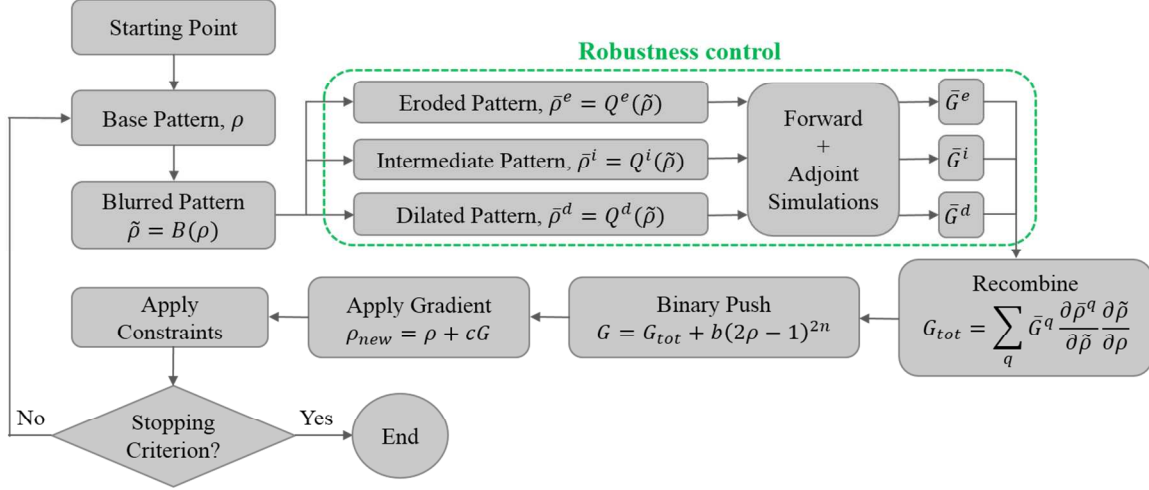


Figure S3. Flow chart of the iterative optimization implementation. Over each iteration, forward and adjoint simulations are performed for the eroded, intermediate, and dilated patterns and produce values of G , which corresponds to the gradient of the figure of merit, $\partial(\text{FoM})/\partial\epsilon$. These values are then used to modify the dielectric constant at all points of the device.

Dielectric constants within the device. During the topology optimization, the dielectric constant at all points in the device can range in continuous fashion between $\epsilon_{\text{high}} = \epsilon_{\text{Si}}$ and $\epsilon_{\text{low}} = \epsilon_{\text{air}}$. For a given iteration u , the device is encoded at all spatial locations \mathbf{r}_i with a real number $\rho_u(\mathbf{r}_i) \in [0,1]$, such that the dielectric constant at each point is given by $\epsilon_u(\mathbf{r}_i) = \rho_u(\mathbf{r}_i)\epsilon_{\text{high}} + (1 - \rho_u(\mathbf{r}_i))\epsilon_{\text{low}}$.

Robustness Control. In order to eliminate small features and create devices that are robust to fabrication error, we employ the method of Ref. [30]. At the beginning of iteration u , a blurring function B_u is applied to the device ρ_u , $B_u: \mathbf{R}^N \rightarrow \mathbf{R}^N$, where N is the total number of points in the device:

$$B_u(\rho_u(\mathbf{r}_i)) = \frac{\sum_{j \in N_e} [(R_u - \|r_j - r_i\|) \rho_u(\mathbf{r}_j)]}{\sum_{j \in N_e} (R_u - \|r_j - r_i\|) \rho_u(\mathbf{r}_j)} = \tilde{\rho}_u(\mathbf{r}_i), \quad N_e = \{j \mid \|r_j - r_i\| \leq R_u\} \quad (\text{S4-1})$$

R_u is the blurring radius and can be iteration-dependent. This blurred geometry is then split into three separate geometric versions $\tilde{\rho}_u^q(r_i)$, where $q \in \{E, I, D\}$ corresponds to the *eroded*, *intermediate*, and *dilated* devices (see Figure S4).

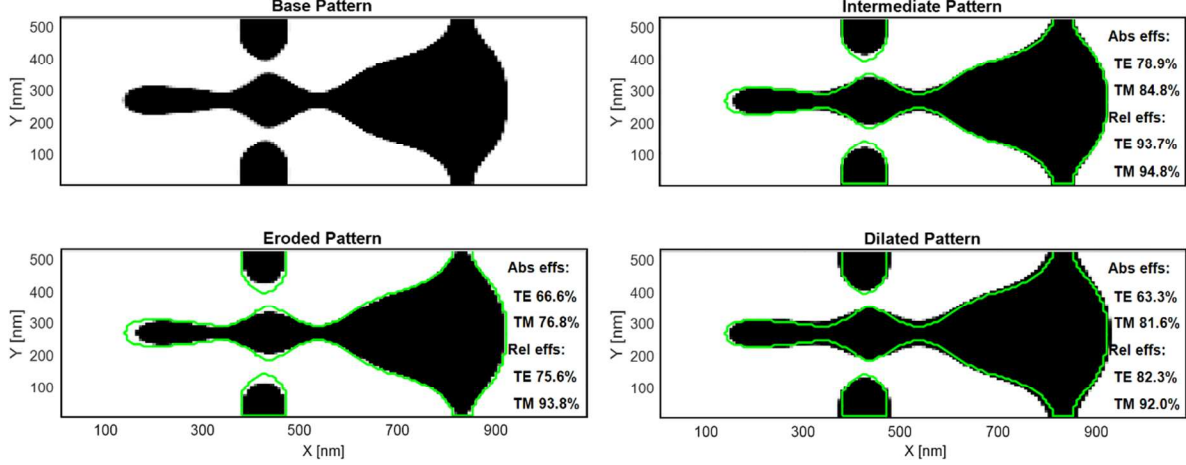


Figure S4. Example of a base pattern and its three blurred patterns. The design is the 75-degree metagrating shown in Figure 1b of the main text. The green curve represents the boundary of the base pattern.

The intermediate pattern represents the ideal pattern for fabrication, and the eroded and dilated patterns represent devices that are over-etched and under-etched, respectively, during fabrication. These geometric variants of the device can be mathematically described as:

$$\tilde{\rho}_u^q(r_i) = \begin{cases} \eta_u^q \{ \exp[-\beta_u(1 - \tilde{\rho}_u(r_i)/\eta_u^q)] - (1 - \tilde{\rho}_u(r_i)/\eta_u^q) \exp(-\beta_u) \}, & 0 \leq \tilde{\rho}_u(r_i) \leq \eta_u^q \\ (1 - \eta_u^q) \{ 1 - \exp[-\beta_u(\tilde{\rho}_u(r_i) - \eta_u^q)/(1 - \eta_u^q)] \} + (\tilde{\rho}_u(r_i) - \eta_u^q)/(1 - \eta_u^q) e^{-\beta_u}, & \eta_u^q < \tilde{\rho}_u(r_i) \leq 1 \end{cases} \quad (\text{S4-2})$$

β_u is the iteration-dependent sharpness of the threshold function, and η_u^q is the cutoff value of $\tilde{\rho}_u$ at which the threshold is applied, such that $\eta_u^E > 0.5$, $\eta_u^I = 0.5$, and $\eta_u^D < 0.5$.

Once the forward and adjoint calculations are performed for all three geometric variants of the device, $\bar{G}^q(r_i) = \partial \text{FoM}^q / \partial \epsilon$ can be calculated for each geometry. A singular $\partial(\text{FoM}) / \partial \epsilon$ that can be applied to the base pattern and that combines these three \bar{G}^q can be expressed as:

$$G_{tot}(r_i) = \sum_q \sum_{e \in N_i} \bar{G}^q(r_e) \frac{\partial \tilde{\rho}_u^q(r_e)}{\partial \tilde{\rho}_u(r_e)} \frac{\partial \tilde{\rho}_u(r_e)}{\partial \rho(r_i)} \quad (\text{S4-3})$$

Once this gradient is calculated, a bias function $Y_u(\rho_u(r_i))$ is added, which is used to slowly push the pattern towards a binary structure (*i.e.*, $\rho_u(r_i) = [0, 1]$). This bias function increases in strength as the full iterative optimization process nears completion.

In the case of a multi-functional device with M functions, each with $G_m(r_i) \equiv \partial \text{FoM}_m / \partial \epsilon$, there are different ways to combine G_m into a single G . Two such methods are:

$$\begin{cases} G(r_i) = \sum_m G_m(r_i) \\ G(r_i) = \sum_m G_m(r_i)(T_m^{tgt} - T_m) \end{cases} \quad (\text{S4-4})$$

The top method optimizes for the total combined power going into all targetted diffraction channels. The bottom method minimizes the mean squared error for a set of targeted power transmission coefficients associated with each diffraction channel, T_m^{tgt} .

Removal of small dielectric features. In order to remove tiny nanoscale features in the device design, we apply a circular spatial blurring filter to the material distribution $\rho_u(r_i)$ every few tens of iterations. For our designs in the main text, the diameter of this circular blurring filter is approximately 80nm, and filtering is performed every 40 iterations. This filtering results in immediate reductions in efficiency, which can be visualized as sharp dips in Figure 1d of the main text.

5. Coupled Bloch mode theory for grating analysis

The dynamics of Bloch mode coupling and propagation in metagratings can be described using coupled Bloch mode analysis (CBMA). CBMA involving the Bloch modes in grating-like structures has been previously adopted to produce in-depth physical insight into the diffraction process in dielectric gratings,²⁷ and it has more recently been used to explain the physics of highly reflective deep lamellar gratings.²⁸ In CBMA, the electromagnetic fields in the air superstrate above the grating (*i.e.*, region I in Figure S5a) and the SiO₂ substrate below the grating (*i.e.*, region III in Figure S5a) can be expanded by Fourier harmonics (*i.e.*, Rayleigh or planewave expansion). The electromagnetic fields inside the periodic metagrating (*i.e.*, region II in Figure S5a) are expanded into a set of N Bloch modes.

The metagrating can be treated as a vertically-oriented Fabry Perot cavity, in which the Bloch modes bounce between the air-metagrating interface and SiO₂-metagrating interface (Figure S5b). As an individual Bloch mode (indexed as mode j) interacts with an interface, three types of processes can occur. First, the mode can transmit out of the cavity and couple to the far-field diffraction channels in regions I or III. Second, the mode can reflect from the interface and propagate in the opposite direction in region II. Third, the mode may couple with and exchange energy with the other $N-1$ Bloch modes in region II. These coupling dynamics at the top and bottom metagrating interfaces are depicted in Figures S5c and S5d. The interaction of the incident plane wave with the bottom metagrating interface shows similar coupling processes and is depicted in Figure S5e.

The Bloch modes include propagating modes, which possess purely real-valued n_{eff} (for lossless materials), and evanescent modes, which possess very high imaginary-valued n_{eff} and exponentially decay along the propagation direction. The metagratings presented here are much thicker than the decay length of the evanescent modes. As such, the propagating modes are the principal modes responsible for energy transport within the metagrating and for energy funneling into the far-field diffractive channels. This approximation is legitimate as long as the evanescent Bloch modes are effectively damped by the relatively thick metagrating.^{28,36}

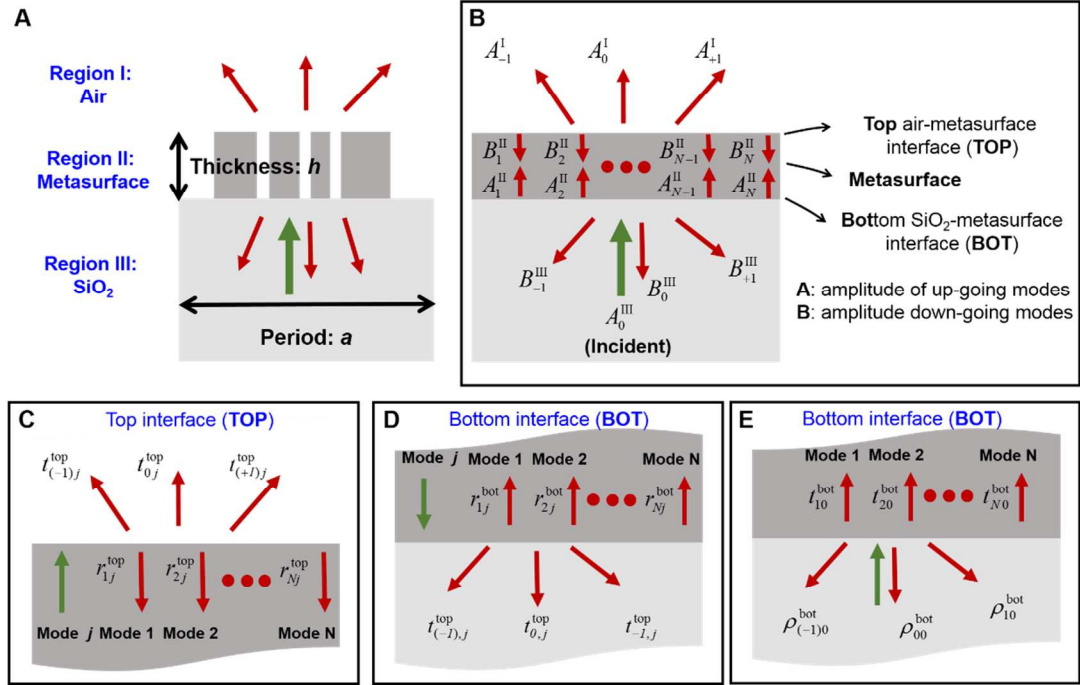


Figure S5. Bloch mode coupling in a metagrating. **a)** Schematic of a metagrating illuminated by an incident beam through the substrate (green arrow), which produces light beams emitted into discrete diffraction channels (red arrows). **b)** Dynamic picture of Bloch mode transport and coupling processes in the metagrating. **c)** Detailed schematic of the mode-coupling processes at the air-metagrating interface for the upward-propagating j^{th} Bloch mode. This mode can couple into the diffracted channels in Region I or couple into downward-propagating Bloch modes (including the j^{th} mode). **d)** Detailed schematic of the Bloch mode coupling processes at the metagrating-substrate interface for the downward-propagating j^{th} Bloch mode. This mode can couple into the diffracted channels in Region III or couple into upward-propagating Bloch modes (including the j^{th} mode). **e)** Detailed schematic of the mode-coupling processes driven by the incident wave at the metagrating-substrate interface. The incident wave can couple into the diffracted channels in Region III or into upward-propagating Bloch modes.

Mathematically, CBMA is explicitly derived based on the N Bloch modes (usually propagating modes) bouncing back and forth within the metagrating, which can be considered as a Fabry-Perot cavity. We denote the effective mode index of the j^{th} Bloch mode as n_j and its propagation delay over a single trip inside the metagratings as $\phi_j = \exp(ik_0 n_j h)$. We define the excitation coefficients of the i^{th} Bloch mode (or n^{th} diffracted order) by the j^{th} Bloch mode as $r_{ij}^{\text{top/bot}}$ (or $t_{nj}^{\text{top/bot}}$) at the top/bottom interface, and the excitation coefficient of the m^{th} far-field diffracted order by the n^{th} order as $\rho_{mn}^{\text{top/bot}}$. Reciprocity ensures certain equality relations such as $r_{ij}^{\text{top/bot}} = r_{ji}^{\text{top/bot}}$, $t_{ij}^{\text{top/bot}} = t_{ji}^{\text{top/bot}}$ and $\rho_{mn}^{\text{top/bot}} = \rho_{nm}^{\text{top/bot}}$. At the metagrating-substrate interface, we have the relation:

$$\begin{bmatrix} A_1^{\text{II}} \\ A_2^{\text{II}} \\ \vdots \\ A_{N-1}^{\text{II}} \\ A_N^{\text{II}} \end{bmatrix} + R^{\text{bot}} \begin{bmatrix} B_1^{\text{II}} \\ B_2^{\text{II}} \\ \vdots \\ B_{N-1}^{\text{II}} \\ B_N^{\text{II}} \end{bmatrix} = T^{\text{bot}} \begin{bmatrix} A_0^{\text{III}} \\ A_0^{\text{III}} \\ \vdots \\ A_0^{\text{III}} \\ A_0^{\text{III}} \end{bmatrix} \quad (\text{S5-1})$$

With:

$$R^{\text{bot}} = \begin{bmatrix} r_{11}^{\text{bot}} \phi_1 & r_{12}^{\text{bot}} \phi_2 & \cdots & r_{1(N-1)}^{\text{bot}} \phi_{N-1} & r_{1N}^{\text{bot}} \phi_N \\ r_{21}^{\text{bot}} \phi_1 & r_{22}^{\text{bot}} \phi_2 & \cdots & r_{2(N-1)}^{\text{bot}} \phi_{N-1} & r_{2N}^{\text{bot}} \phi_N \\ \vdots & \vdots & \ddots & \vdots & \vdots \\ r_{(N-1)1}^{\text{bot}} \phi_1 & r_{(N-1)2}^{\text{bot}} \phi_2 & \cdots & r_{(N-1)(N-1)}^{\text{bot}} \phi_{N-1} & r_{(N-1)N}^{\text{bot}} \phi_N \\ r_{N1}^{\text{bot}} \phi_1 & r_{N2}^{\text{bot}} \phi_2 & \cdots & r_{N(N-1)}^{\text{bot}} \phi_{N-1} & r_{NN}^{\text{bot}} \phi_N \end{bmatrix} \text{ and } T^{\text{bot}} = \begin{bmatrix} t_{10}^{\text{bot}} & 0 & 0 & 0 & 0 \\ 0 & t_{20}^{\text{bot}} & 0 & 0 & 0 \\ 0 & 0 & \ddots & 0 & 0 \\ 0 & 0 & 0 & t_{(N-1)0}^{\text{bot}} & 0 \\ 0 & 0 & 0 & 0 & t_{N0}^{\text{bot}} \end{bmatrix}$$

Similarly, at the top air-metagrating interface, we have:

$$R^{\text{top}} \begin{bmatrix} A_1^{\text{II}} \\ A_2^{\text{II}} \\ \vdots \\ A_{N-1}^{\text{II}} \\ A_N^{\text{II}} \end{bmatrix} + \begin{bmatrix} B_1^{\text{II}} \\ B_2^{\text{II}} \\ \vdots \\ B_{N-1}^{\text{II}} \\ B_N^{\text{II}} \end{bmatrix} = \begin{bmatrix} 0 \\ 0 \\ \vdots \\ 0 \\ 0 \end{bmatrix} \quad (\text{S5-2})$$

With:

$$R^{\text{top}} = \begin{bmatrix} r_{11}^{\text{top}} \phi_1 & r_{12}^{\text{top}} \phi_2 & \cdots & r_{1(N-1)}^{\text{top}} \phi_{N-1} & r_{1N}^{\text{top}} \phi_N \\ r_{21}^{\text{top}} \phi_1 & r_{22}^{\text{top}} \phi_2 & \cdots & r_{2(N-1)}^{\text{top}} \phi_{N-1} & r_{2N}^{\text{top}} \phi_N \\ \vdots & \vdots & \ddots & \vdots & \vdots \\ r_{(N-1)1}^{\text{top}} \phi_1 & r_{(N-1)2}^{\text{top}} \phi_2 & \cdots & r_{(N-1)(N-1)}^{\text{top}} \phi_{N-1} & r_{(N-1)N}^{\text{top}} \phi_N \\ r_{N1}^{\text{top}} \phi_1 & r_{N2}^{\text{top}} \phi_2 & \cdots & r_{N(N-1)}^{\text{top}} \phi_{N-1} & r_{NN}^{\text{top}} \phi_N \end{bmatrix}$$

Combining Eqs.S5-1 and S5-2, we obtain:

$$\begin{bmatrix} A_I^{\text{II}} \\ A_2^{\text{II}} \\ \vdots \\ A_{N-I}^{\text{II}} \\ A_N^{\text{II}} \end{bmatrix} = (I - R^{\text{bot}} R^{\text{top}})^{-I} T^{\text{bot}} \begin{bmatrix} A_0^{\text{III}} \\ A_0^{\text{III}} \\ \vdots \\ A_0^{\text{III}} \\ A_0^{\text{III}} \end{bmatrix} \quad (\text{S5-3})$$

Equation S5-3 provides the amplitudes of the upward propagating Bloch modes inside the metagrating, as excited by the external illumination. The amplitudes of the downward-propagating Bloch modes can be obtained by substituting Eq. S5-3 into Eq. S5-2. Then the m^{th} diffracted order in Region I can be written as:

$$A_m^{\text{I}} = \sum_j t_{m,j}^{\text{top}} A_j^{\text{II}} \phi_j. \quad (\text{S5-4})$$

The amplitudes of the m^{th} diffracted orders in region III can be written as:

$$A_m^{\text{III}} = \sum_j t_{m,j}^{\text{bot}} B_j^{\text{II}} \phi_j + \rho_{m0} A_0^{\text{III}}. \quad (\text{S5-5})$$

In Equations S5-4 and S5-5, the far-field diffracted channels are written as the coherent summation over all the propagating Bloch modes inside the metagrating, and they allow us to examine Bloch mode interference as they couple into the diffraction channels. We note that if only one Bloch mode is kept in Equations S5-4 and S5-5, these equations reduce to the classical Fabry-Perot formulas³⁶ for a single mode in a periodic medium.

6. Mode analysis: topology-optimized 75 degree deflector

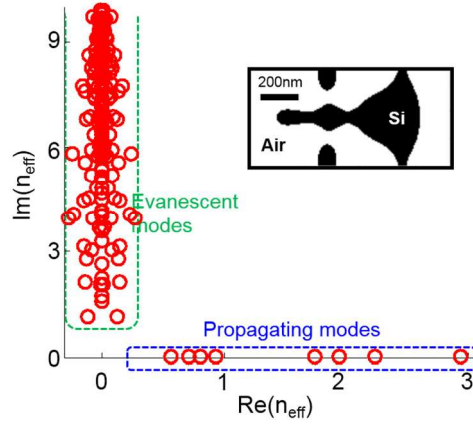


Figure S6. Effective indices n_{eff} of the Bloch modes in the 75 degree deflector for TM polarization. Each red circle marker represents a Bloch mode identified by the RCWA solver. There are 8 propagating modes, contained within the blue box, which have negligible $\text{Im}(n_{\text{eff}})$. The field profiles of these modes are plotted in Figure 2b of the main text. The evanescent modes are contained in the open green curve. All of these modes have large imaginary parts and decay strongly with a propagation length less than or equal to the metagrating thickness.

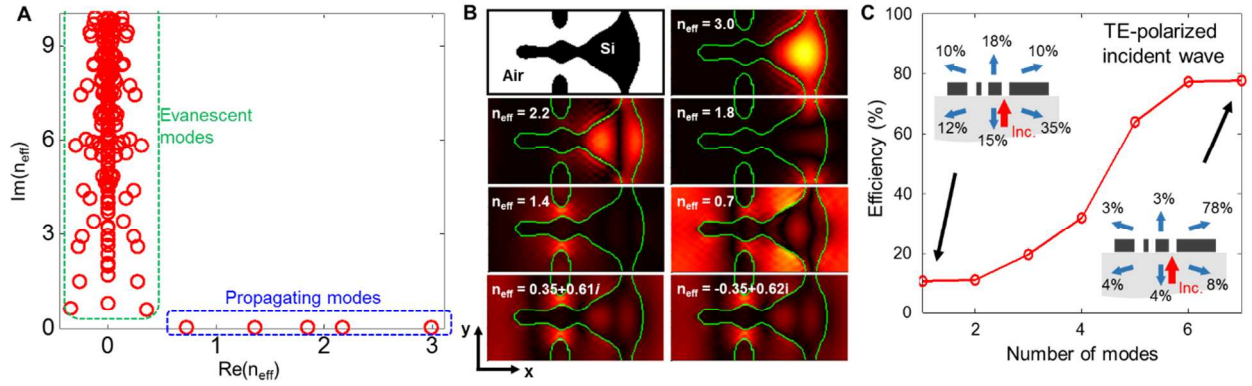


Figure S7. Coupled Bloch mode analysis of the 75 degree metagrating for TE polarization. (a) Effective indices n_{eff} of the TE-polarized Bloch modes of the metagrating, calculated using the RCWA solver. The device supports five propagating modes, contained within the blue box, and many evanescent modes, contained within the open green curve. Most of the evanescent modes have large imaginary parts and strongly decay with a propagation length less than or equal to the metagrating thickness. However, two of the evanescent modes have relatively small imaginary parts and do not strongly decay within the metagrating. These two evanescent modes, together with the five propagating modes, contribute to the deflection efficiency of the metagrating. (b) $|E|$ profiles of the seven Bloch modes that contribute to the deflection efficiency of the metagrating. The effective mode refractive indices n_{eff} are listed, and outlines of the silicon structure are drawn in green. (c) Plot of deflection efficiency of the simulated metagrating as a function of number of modes included in the grating efficiency calculation, for a TE-polarized incident beam. For one mode, the diffractive optical properties of the Bloch mode with $n_{\text{eff}} = 3.0$ is included, and only 10% of the light is deflected into the desired grating order (inset, top left). Note that the total efficiency from all diffraction channels adds to 100%. As more modes are included (added in order of decreasing n_{eff}), the deflection efficiency of the metagrating gradually increases. When all seven modes are included, the deflection efficiency into the desired channel is 78% (inset, bottom right).

7. Mode analysis: Metagrating deflector based on effective refractive index design concept

In this section, we analyze the modes of a 75 degree deflector design based on the effective refractive index concept.^{6,7} This design method is represented by the light blue curve in Figure 1a of the main text. For this large deflection angle, the device period is small, such that there is space for only two TiO_2 square pillars (see Figure S8a, inset). This two-pillar design supports 60% and 30% absolute efficiencies for TM- and TE-incident polarized waves, respectively.

We perform coupled Bloch mode analysis for this metagrating for TM-polarized incident light and find that the metagrating supports three propagating modes (Figure S8a). As shown in Figure S8b, the field profiles of two of the modes ($n_{\text{eff}} = 1.61$ and 1.21) are mostly confined in the nanopillars, in good agreement with the effective medium approximation approach (6, 7). The third propagating mode has an effective index $n_{\text{eff}} \sim 1$ and its field is mostly distributed in air.

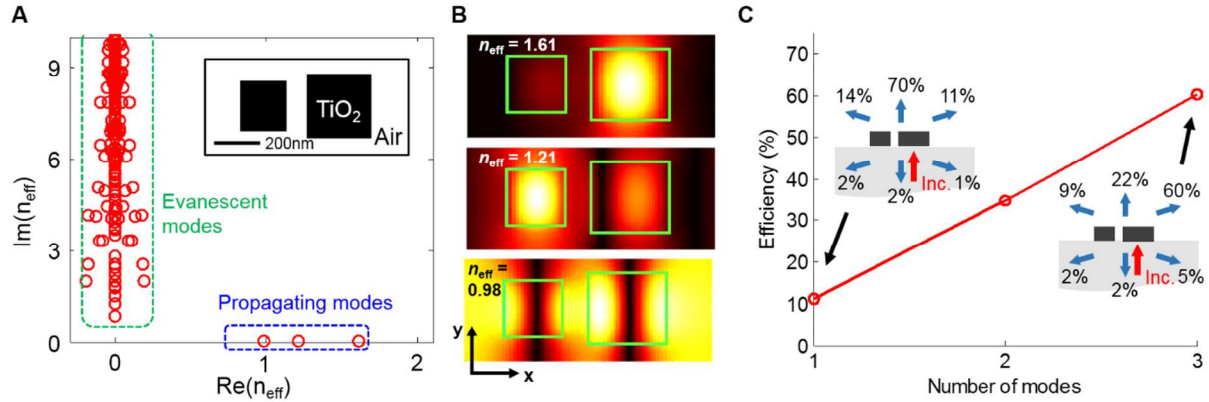


Figure S8. Coupled Bloch mode analysis of a 75-degree deflector made of two TiO_2 square pillars. This grating design is chosen from the gratings designed by the effective medium approach shown in Figure 1 in the main text and is analyzed for incident TM-polarized light. (a) The grating layout and its Bloch modes at TM polarization. (b) $|\mathbf{H}|$ of the three propagating modes. (c) Deflection efficiency as a function of number of modes. For one mode, the diffractive optical properties of the Bloch mode with $n_{\text{eff}} = 1.61$ is included, and only 11% of the light is deflected into the desired direction (inset, top left). As more modes are included (added in order of decreasing n_{eff}), the deflection efficiency of the metagrating gradually increases. When all three modes are accounted for, the deflection efficiency into the desired channel is 60% (inset, bottom right).

8. Incident angle sensitivity of the topology-optimized 75 degree deflector

In this section, we evaluate the impact of variations in angle of incidence on the performance of our 75 degree deflector from Figure 3 of the main text. These variations in incidence angle arise experimentally because our incident beam is weakly focused on the sample.

Plots of simulated absolute efficiency as a function of incidence angle (θ_{inc}) for the device are displayed in Figure S9. For the 75 degree metagrating, the calculation is performed for θ_{inc} ranging from -7 to +1.3 degrees from the glass substrate, which corresponds to -10 to +2 degrees in air. The +2 degree angle is a limit that arises from the cutoff of the diffracted beam at larger incident angles.

Experimentally, our incident beam has incident angles that show a *Gaussian distribution* (not a uniform distribution) over a narrow angular range spanning from -1 to +1 degrees in air (see Figure S1b). This is sufficient to avoid efficiency drop (cutoff) shown in Figure S9 due to deviation of the angle of the incident light. As such, we expect variations in incidence angle to minimally impact the efficiencies of our devices.

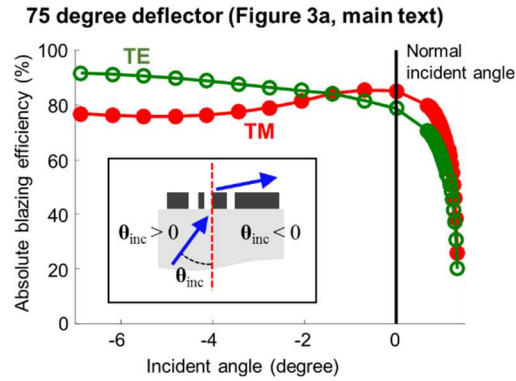


Figure S9. Absolute deflection efficiency as a function of different incident angles. The simulated plots for the 75 degree deflector are shown.

9. Additional images and experimental spectra of the topology-optimized 75 degree deflector

75 degree deflector (Figure 3a, main text)

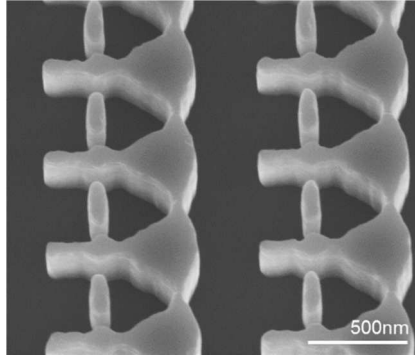


Figure S10. Tilted scanning electron microscopy images of the metagrating from the main text. The sidewall profile of the device is vertical.

75 degree deflector (Figure 3a, main text)

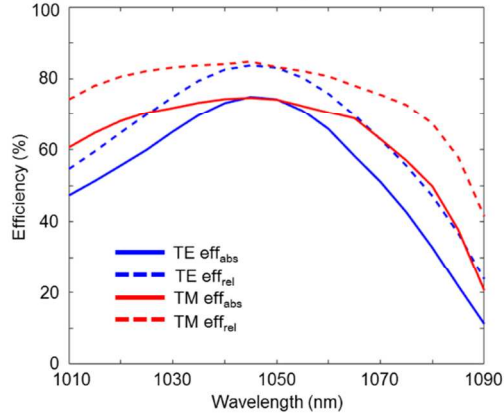


Figure S11. Experimental metagrating efficiencies as a function of incident wavelength for the 75 degree deflector from Figure 3 of the main text.

10. Analysis of the accuracy of rigorous coupled-wave analysis simulations

In this section, we analyze the convergence of the rigorous coupled-wave analysis (RCWA) simulations. We use the open-source RCWA code Reticolo²⁹ as the electromagnetic solver for the optimization process, which Fourier expands the electromagnetic fields in our system. The numerical inaccuracies of RCWA mainly arise due to inevitable truncation of these Fourier series in the simulation.

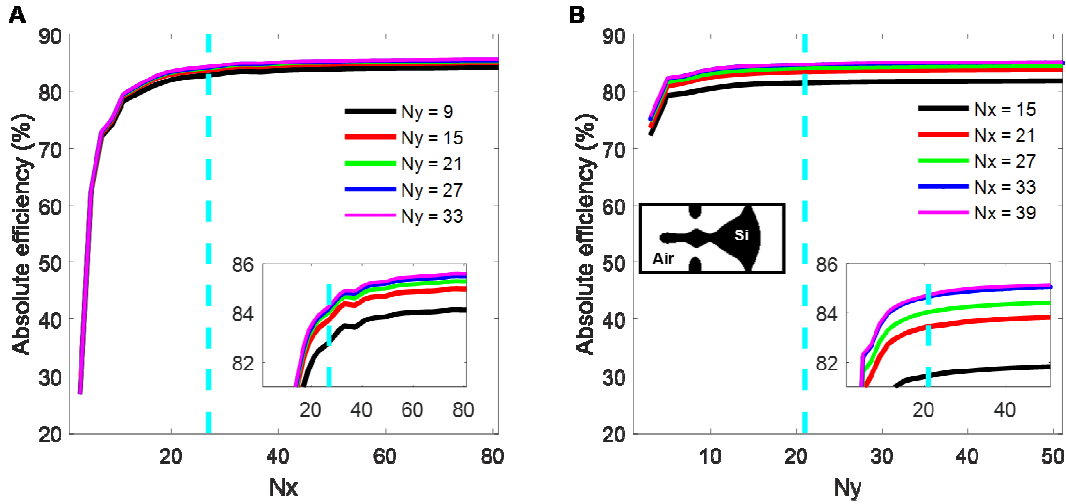


Figure S12. Numerical convergence test. Convergence tests for the blazing efficiency of the 75 degree metagrating in the main text. **a)** The results for varying N_x values with several fixed N_y values. **b)** The the results for varying N_y values with several fixed N_x values. The vertical cyan lines mark the N_x or N_y values used in our optimization. The inset in **b)** shows the metagrating layout under test.

To evaluate the accuracy of our numerical results, we simulate the 75 degree blazed metagrating from the main text (see inset in Figure S12b) with progressively increasing numbers (N_x or N_y) of Fourier harmonics in the computation. Here, our Fourier series goes from $-(N-1)/2$ to $+(N-1)/2$ for each axis. The plots in Figure S12 show the absolute deflection efficiencies of the metagrating with differing numbers of Fourier harmonics. Here, we fix the number of Fourier harmonics for one axis and vary the number of Fourier harmonics for the other axis. Figure S12a show the convergence tests of absolute efficiency for varying N_x values with several fixed N_y values. When N_y is large enough ($N_y > 15$), all the calculations converge to within 0.5% of the same value. When $N_y > 15$ and $N_x = 27$, all of the calculations produce values that are within 1% of the accurate converged value. Similarly, the simulation results shown in Figure S12b indicate that when $N_x > 21$ and $N_y = 21$, all of the calculations produce values that are within 1% of the accurate converged value. Therefore, simulations with $N_x = 27$ and $N_y = 21$ produce results with with numerical accuracies within $\sim 1\%$, and we use these values for our inverse design procedure. We have checked that all computational results presented in this study display similar numerical accuracies.

11. Analysis of the topology-optimized 75 degree deflector using finite-element-method (COMSOL) calculations

In this section, we use the finite-element-method software COMSOL Multiphysics (version 5.0) to simulate the performance of our topology-optimized metagratings. COMSOL is an established, commercial software package that is suitable for modeling curvilinear geometries. For this analysis, we simulate the 75 degree metagrating from the main text. We approximate the curvilinear grating geometry using a combination of simple geometric shapes and combine them using the “*booleans and partitions*” operation in COMSOL. The elementary geometries are delimited by green and red lines in Figure S13. The precise geometric dimensions of these shapes are recorded in Table S2. The corners of all rectangles are rounded and have a radius of curvature of 8 nm.

The deflection efficiencies of a metagrating of this approximate geometry are calculated using COMSOL to be 84% and 79% for TM and TE polarizations, respectively, for a normally incident planewave through the glass substrate. These values are in excellent agreement with our RCWA calculations of the metagrating (85% and 79% for TM and TE polarizations, respectively). This agreement between COMSOL and RCWA simulations is another indication that RCWA can simulate our curvilinear, topology-optimized geometries with high accuracy.

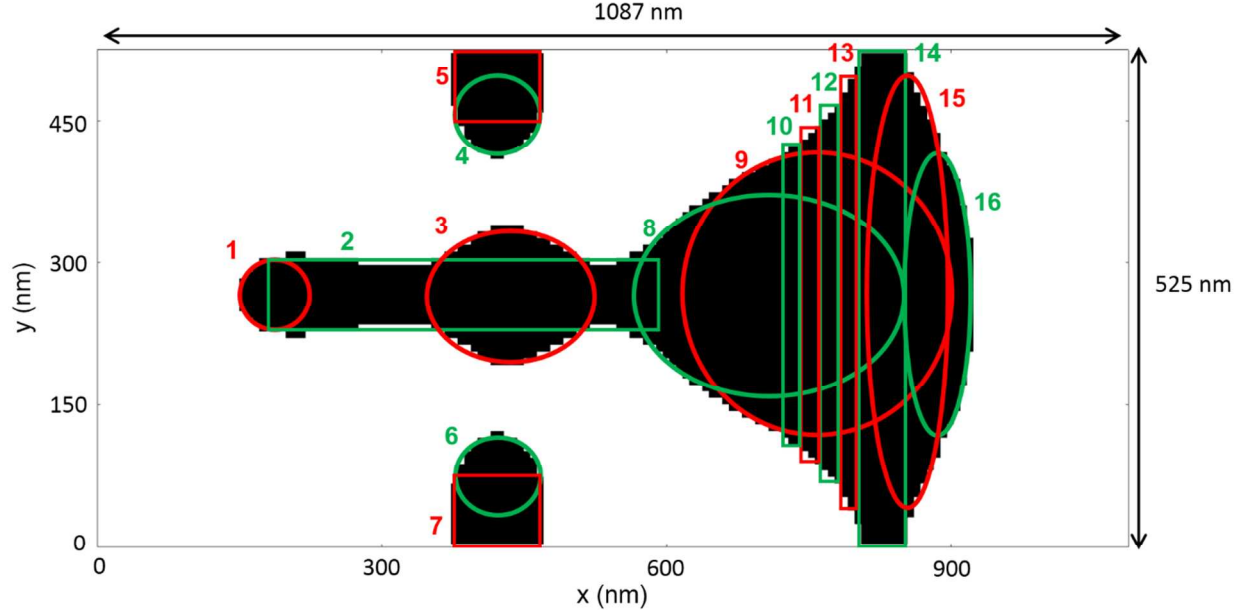


Figure S13. Top view of a single period of a 75 degree metagrating layout used in COMSOL simulations. The layout shown in black is that used in RCWA simulations. The approximate layout used in COMSOL consists of a combination of sixteen ellipses and rectangles, which are shown here outlined by red and green curves. The dimensions of the grating period along x and y are 1087nm and 525nm, respectively.

Table S2. Details of the elementary geometries (units: nm)

Geometry	Size	Center position
1: ellipse	Axis Length 74 x 74	(185, 262.5)
2: rectangle	Side Length 412 x 74	(385.5, 262.5)
3: ellipse	Axis Length 177.5 x 138	(432, 262.5)
4: ellipse	Axis Length 91 x 82.5	(419, 457.5)
5: rectangle	Side Length 91 x 74	(419, 488)
6: ellipse	Axis Length 91 x 82.5	(419, 67.5)
7: rectangle	Side Length 91 x 74	(419, 37)
8: ellipse	Axis Length 285 x 213	(710, 262.5)
9: ellipse	Axis Length 285 x 299	(758.5, 262.5)
10: rectangle	Side Length 18 x 320	(731, 262.5)
11: rectangle	Side Length 19 x 355	(749, 262.5)
12: rectangle	Side Length 22 x 399	(768, 262.5)
13: rectangle	Side Length 20 x 458.5	(788, 262.5)
14: rectangle	Side Length 52 x 525	(824, 262.5)
15: ellipse	Axis Length 85.5 x 458.5	(854.5, 262.5)
16: ellipse	Axis Length 71 x 299	(884, 262.5)

12. Geometrical parameters of the metagrating deflectors in Figure 1a

(i) Details of metagratings based on the “Effective medium” method

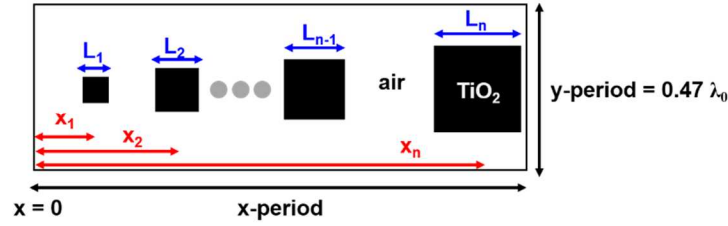


Figure S14. Sketch of the metagratings based on “Effective medium” method.

Table S3. Parameters of the metagratings designed with the “Effective medium” method

Deflection angle (deg)	x-period (λ_0)	$x_1, x_2, \dots x_n$ (λ_0)	$L_1, L_2, \dots L_n$ (λ_0)	Thickness (λ_0)
9.4	6.1	0.700 1.170 1.640 2.110 2.580 3.050 3.520 3.990 4.460 4.930 5.400 5.870	0.130 0.170 0.190 0.220 0.230 0.250 0.260 0.280 0.290 0.300 0.320 0.330	1.40
10.1	5.7	0.710 1.190 1.660 2.140 2.610 3.090 3.560 4.040 4.510 4.980 5.460	0.130 0.170 0.200 0.220 0.240 0.260 0.270 0.290 0.300 0.320 0.330	1.39
11.1	5.2	0.710 1.180 1.650 2.130 2.600 3.070 3.550 4.020 4.490 4.960	0.140 0.180 0.210 0.230 0.250 0.270 0.280 0.300 0.320 0.330	1.37
12.3	4.7	0.710 1.180 1.650 2.120 2.590 3.060 3.530 4.000 4.470	0.140 0.180 0.220 0.240 0.260 0.280 0.290 0.310 0.330	1.36
13.8	4.2	0.700 1.170 1.630 2.100 2.570 3.030 3.500 3.970	0.150 0.190 0.220 0.250 0.270 0.290 0.310 0.330	1.34
15.3	3.8	0.710 1.190 1.660 2.140 2.610 3.090 3.56	0.160 0.200 0.230 0.26 0.280 0.310 0.330	1.32
17.6	3.3	0.710 1.180 1.650 2.120 2.590 3.060	0.170 0.220 0.250 0.280 0.300 0.330	1.30
20.5	2.85	0.710 1.190 1.660 2.140 2.610	0.180 0.230 0.270 0.300 0.330	1.26
25.2	2.35	0.710 1.180 1.650 2.12	0.190 0.250 0.290 0.330	1.21
32.7	1.85	0.690 1.160 1.620	0.220 0.280 0.330	1.13
45.6	1.4	0.700 1.170	0.250 0.330	1.01
50.3	1.30	0.480 0.910	0.250 0.330	1.01
61.3	1.14	0.380 0.780	0.250 0.330	1.01
72.2	1.05	0.310 0.700	0.250 0.330	1.01
81.9	1.01	0.280 0.670	0.250 0.330	1.01
85.0	1.004	0.280 0.670	0.250 0.330	1.01

(ii) Details of metagratings based on the “Transmit array” method

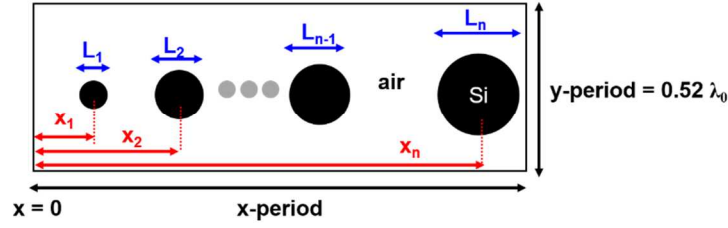


Figure S15. Sketch of the metagratings based on “Transmit array” method.

Table S4. Parameters of the metagratings designed with the “Transmit array” method

Deflection angle (deg)	x-period (λ_0)	$x_1, x_2, \dots x_n$ (λ_0)				$L_1, L_2, \dots L_n$ (λ_0)				Thickness (λ_0)
9.2	6.29	0.262	0.786	1.310	1.834	0.152	0.182	0.195	0.203	0.59
		2.358	2.882	3.406	3.930	0.210	0.215	0.220	0.225	
		4.454	4.978	5.502	6.026	0.232	0.241	0.265	0.296	
10.0	5.8	0.262	0.786	1.309	1.833	0.154	0.184	0.198	0.206	0.59
		2.356	2.880	3.404	3.927	0.212	0.217	0.223	0.230	
		4.451	4.975	5.498		0.238	0.260	0.295		
11.0	5.22	0.261	0.783	1.305	1.827	0.157	0.187	0.200	0.208	0.59
		2.349	2.871	3.393	3.915	0.214	0.221	0.227	0.236	
		4.437	4.959			0.253	0.293			
12.3	4.7	0.262	0.785	1.308	1.832	0.160	0.190	0.202	0.211	0.59
		2.355	2.878	3.402	3.925	0.217	0.225	0.233	0.247	
		4.448				0.291				
13.8	4.19	0.262	0.786	1.309	1.833	0.163	0.193	0.205	0.213	0.59
		2.357	2.881	3.404	3.928	0.221	0.230	0.244	0.288	
15.8	3.7	0.262	0.785	1.309	1.833	0.166	0.196	0.209	0.217	0.59
		2.356	2.880	3.403		0.227	0.240	0.285		
18.6	3.14	0.262	0.785	1.308	1.832	0.171	0.200	0.212	0.223	0.59
		2.355	2.878			0.236	0.282			
22.6	2.6	0.184	0.923	1.443	1.963	0.176	0.204	0.217	0.231	0.59
		2.392				0.277				
28.4	2.10	0.263	0.788	1.313	1.838	0.182	0.210	0.225	0.265	0.59
39.6	1.6	0.262	0.785	1.308		0.190	0.217	0.247		0.59
50.3	1.3	0.325	0.975			0.200	0.236			0.59
65.4	1.10	0.275	0.825			0.200	0.236			0.59
72.3	1.05	0.263	0.788			0.200	0.236			0.59
80.0	1.015	0.254	0.762			0.200	0.236			0.59
85.0	1.004	0.251	0.753			0.200	0.236			0.59

(iii) Details of metagratings based on the “Geometric phase” method

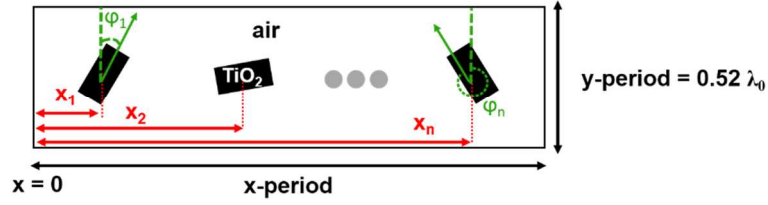


Figure S16. Sketch of the metagratings based on “Geometric phase” method.

Table S5. Parameters of the metagratings designed with the “Geometric phase” method

Deflection angle (deg)	x-period (λ_0)	$x_1, x_2, \dots x_n$ (λ_0)				$\varphi_1, \varphi_2, \dots \varphi_n$ (deg)				Thickness (λ_0)
10.1	5.70	0.259	0.778	1.296	1.815	8.2	24.6	40.9	57.3	1.48
		2.333	2.852	3.370	3.889	73.6	90	106.4	122.7	
		4.407	4.926	5.444		139.1	155.5	171.8		
13.9	4.15	0.259	0.778	1.296	1.815	11.3	33.8	56.3	78.8	1.48
		2.333	2.852	3.370	3.889	101.3	123.8	146.3	168.8	
16.0	3.63	0.259	0.778	1.296	1.815	12.9	38.6	64.3	90	1.48
		2.333	2.852	3.370		115.7	141.4	167.1		
18.7	3.11	0.259	0.778	1.296	1.815	15.0	45.0	75.0	105.0	1.48
		2.333	2.852			135.0	165.0			
22.7	2.59	0.259	0.778	1.296	1.815	18.0	54.0	90.0	126.0	1.48
		2.333				162.0				
28.8	2.07	0.259	0.778	1.296	1.815	22.5	67.5	112.5	157.5	1.48
40.0	1.56	0.259	0.778	1.296		30.0	90.0	150.0		1.48
45	1.41	0.236	0.707	1.179		30.0	90.0	150.0		1.48
50	1.31	0.218	0.653	1.088		30.0	90.0	150.0		1.48
60	1.15	0.289	0.866			45	135			1.48
74.6	1.04	0.259	0.778			45	135			1.48
80	1.02	0.254	0.762			45	135			1.48
85	1.004	0.251	0.753			45	135			1.48

(iv) Geometrical details of the Echelle gratings with sawtooth profiles

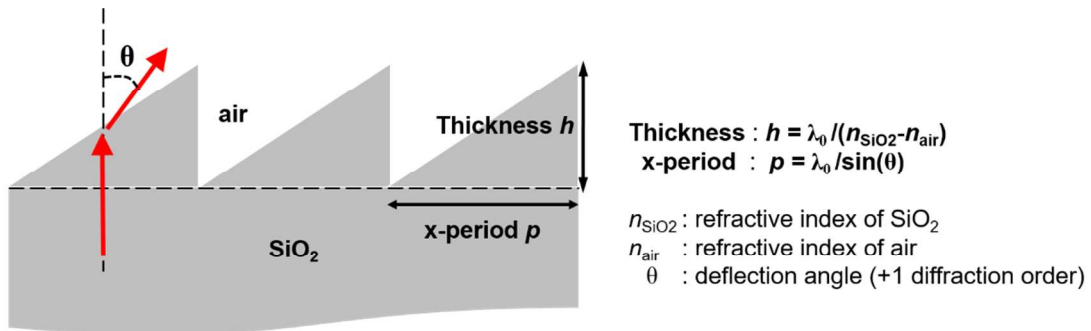


Table S17. Parameters of the Echelle gratings of sawtooth profiles.

13. Description of Movie S1

Movie S1 shows the top view of the topology-optimized grating from Figure 1b of the main text over the course of a full optimization procedure. The shading corresponds to dielectric constant values between those of silicon and air. The images and efficiency data in the movie are used to construct Figure 1d of the main text.

14. References

- 33 Snyder, A. W. & Love, J. *Optical Waveguide Theory*. (Kluwer Academic Publishers, 1983).
- 34 Yang, J., Hugonin, J.-P. & Lalanne, P. Near-to-Far Field Transformations for Radiative and Guided Waves. *ACS Photonics* **2016**, *3*, 395-402.
- 35 Yang, J., Giessen, H. & Lalanne, P. Simple Analytical Expression for the Peak-Frequency Shifts of Plasmonic Resonances for Sensing. *Nano Lett.* **2015**, *15*, 3439-3444.
- 36 Yang, J., Sauvan, C., Paul, T., Rockstuhl, C., Lederer, F. & Lalanne, P. Retrieving the effective parameters of metamaterials from the single interface scattering problem. *Appl. Phys. Lett.* **2010**, *97*, 061102.